Geophysical Research Letters

RESEARCH LETTER
10.1029/2022GL101241

Fault Roughness Promotes Earthquake-Like Aftershock Clustering in the Lab

Thomas H. W. Goebel[1], **Emily E. Brodsky**[2], **and Georg Dresen**[3]

[1]Center for Earthquake Research and Information, University of Memphis, Memphis, TN, USA, [2]Department of Earth Sciences, University of California, Santa Cruz, CA, USA, [3]German Research Centre for Geosciences, Potsdam, Germany

Key Points:

- Aftershock productivity in lab experiments is directly correlated with residual stress on the fault after abrupt slip
- Both residual stress and aftershock productivity are substantially higher on rough than on smooth faults
- Spatio-temporal clustering of laboratory seismicity in the transitional frictional regime is similar to Southern California seismicity

Supporting Information:

Supporting Information may be found in the online version of this article.

Correspondence to:

T. H. W. Goebel,
thgoebel@memphis.edu

Citation:

Goebel, T. H. W., Brodsky, E. E., & Dresen, G. (2023). Fault roughness promotes earthquake-like aftershock clustering in the lab. *Geophysical Research Letters*, *50*, e2022GL101241. https://doi.org/10.1029/2022GL101241

Received 13 SEP 2022
Accepted 3 APR 2023

Author Contributions:

Conceptualization: Thomas H. W. Goebel, Emily E. Brodsky, Georg Dresen
Data curation: Thomas H. W. Goebel
Formal analysis: Thomas H. W. Goebel
Funding acquisition: Thomas H. W. Goebel
Methodology: Thomas H. W. Goebel
Resources: Georg Dresen

Abstract Earthquakes rarely occur in isolation but rather as complex sequences of fore, main and aftershocks. Assessing the associated seismic hazard requires a holistic view of event interactions. We conduct frictional sliding experiments on faulted Westerly Granite samples at mid-crustal stresses to investigate fault damage and roughness effects on aftershock generation. Abrupt laboratory fault slip is followed by periods of extended stress relaxation and aftershocks. Large roughness promotes less co-seismic slip and high aftershock activity whereas smooth faults promote high co-seismic slip with few aftershocks. Conditions close to slip instability generate lab-quake sequences that exhibit similar statistical distributions to natural earthquakes. Aftershock productivity in the lab is linearly related to the residual strain energy on the fault which, in turn, is controlled by the level of surface heterogeneity. We conclude that roughness and damage govern slip stability and seismic energy partitioning between fore, main and aftershocks in lab and nature.

Plain Language Summary Earthquakes commonly occur as sequences of fore, main and aftershocks rather than isolated events. A complete assessment of seismic hazard thus requires a holistic view of interactions between seismic events. We investigated such event interactions during frictional experiments on Westerly Granite. The samples contained rough and planar fault surfaces and we investigated seismic events, specifically aftershocks after abrupt laboratory slip. We observed that larger roughness promotes less slip on the fault during macroscopic failure but more aftershock activity. Smooth faults, on the other hand, promote more slip in large events with few aftershocks. The statistical characteristics of small lab-quake sequences and aftershocks are statistically indistinguishable from natural earthquakes. We conclude that roughness and damage govern slip stability and seismic energy partitioning between fore, main and aftershocks in lab and nature.

1. Introduction

Most earthquakes occur as spatially and temporally clustered sequences of events which are linked by a process referred to as triggering. Triggering describes a causal relationship by which preceding events lead to the nucleation of subsequent earthquakes, which is most evident during mainshock-aftershock sequences. Triggered events are commonly detected based on significant rate increase (i.e., inter-event time decrease) and deviation from Poissonian background rates, which is also used to detect triggered aftershocks in the lab (Davidsen et al., 2017). In nature, triggering is observed at many spatial and temporal scales and is thought to control 50%–90% of all earthquake occurrences (Zaliapin & Ben-Zion, 2013).

Triggering may be a fundamental component of the earthquake nucleation process, leading to cascades of foreshocks, mainshocks and aftershocks (Ellsworth & Bulut, 2018; Helmstetter & Sornette, 2003). Underlying processes are thought to involve static and dynamic stresses, viscoelastic relaxation and post-seismic creep, poroelastic effects, sub-critical crack growth and rate-dependent friction (J. Dieterich, 1994; Elst & Brodsky, 2010; Kanamori & Brodsky, 2004; King et al., 1994; Perfettini & Avouac, 2004; Scholz, 1968). The dominant mechanism is difficult to resolve; however consequences of triggering are easily observable. For instance, triggering causes pronounced space-time clustering of earthquakes within about two rupture dimensions from mainshocks (King et al., 1994). Such clustering can be described statistically by power law aftershock-rate and spatial decay (Felzer & Brodsky, 2006; Utsu, 1999) and the total number of aftershocks scales, on average, exponentially with mainshock magnitude (Utsu, 1999). Typical Omori-type aftershock decay is predicted for sudden stress-increase across crack populations governed by (power-law) sub-critical crack growth or rate-and-state friction (J. Dieterich, 1994; Kanamori & Brodsky, 2004). Numerical models also highlight that crustal thickness and fault

damage contribute to Omori-like aftershock decay (Ben-Zion & Lyakhovsky, 2006); however, there is a lack of observational constraints for the coupling between fault damage and aftershocks.

Triggering intensity (i.e., the relative seismicity rate change compared to background) is strongly affected by mainshock magnitude and resulting stress perturbations (Elst & Brodsky, 2010). However, triggering intensity varies by several orders of magnitude even for similar magnitude mainshocks, highlighting that triggering is not solely governed by source characteristics but also crustal conditions (Dascher-Cousineau et al., 2020; Wetzler et al., 2018). Untangling the different contributions to aftershock generation is complicated by observational limitations and crustal heterogeneity in nature.

Laboratory experiments have revealed much about earthquake nucleation but have rarely been able to capture natural stress relaxation processes and aftershocks (Dresen et al., 2020; T. H. W. Goebel et al., 2017; Scholz, 1968). Recent advances in experimental methods and laboratory instrumentation suggests scale-invariant seismogenic deformation and source parameter characteristics (i.e., corner frequency and seismic moment)—at least under certain conditions (McLaskey et al., 2014). This scale-invariance indicates that rupture nucleation and arrest may be controlled by similar processes across a wide range of scales, including the intermediate scale of mining-induced earthquakes (Kwiatek et al., 2011). Laboratory-created fault zones that evolve with cumulative displacements are comprised of hierarchical damage structures, including a core deformation zone and off-fault damage (T. H. W. Goebel, Becker, et al., 2014; T. H. W. Goebel, Candela, et al., 2014).

Here, we investigate fore and aftershock generation over several seismic cycles in the controlled laboratory environment. We start by carefully examining high-resolution acoustic emission (AE) records to identify aftershock sequences based on magnitude differences and seismicity rate decay—analogous to aftershock detection in nature. We then explore primary controls on aftershock behavior, finding that aftershock productivity is strongly correlated with residual stress (i.e., remaining shear stress after abrupt fault slip). This residual stress is modulated by fault roughness, with rough faults generating a broad range of small and large stress drop events and overall higher residual stresses than smooth faults. Note that stress drop here is measured directly by comparing external load cell measurements before and after slip which is different from seismological stress drop estimates based on far-field particle motion. Lastly, we provide an explanation for the observations based on the mechanics of frictional sliding and stick-slip. We observe that normal stress, stiffness and frictional parameters explain the full range of stress drops and associated aftershock behavior.

2. Method

2.1. Experimental Design and Sample Preparation

Triaxial compression experiments were conducted on 14 cylindrical (diameter = 40 and 50 mm, height = 105 mm) Westerly granite samples at confining pressures, P_c between 120 and 150 MPa (Figure S1; Table S1 in Supporting Information S1). All samples were separated from the confining oil by an elastic rubber jacket and loaded axially at a displacement rate of 3×10^{-4} mm/s up to a maximum vertical displacement of $u \sim 6$ mm. An external load cell and two vertical and horizontal strain gauges measured axial force and strain with a sampling rate of 10 Hz.

We generated a range of fault roughness by introducing 30° saw-cuts and fracturing initially intact rocks at $P_c = 75$ MPa. The samples were subsequently reloaded at $P_c = 150$ MPa leading to stick-slip or stable sliding. Fault roughness variations were examined in X-ray computer tomography and white-light interferometry scans, yielding almost two orders of magnitude difference in rms-roughness between smooth (~0.01 mm) and rough faults (~0.6 mm).

2.2. Acoustic Emission Detection and Locations

We analyze active and passive seismic sources using a 16 channel, high-speed data acquisition system (Stanchits et al., 2006). Accurate AE locations were possible due to high-quality automated picks (Figure S4 in Supporting Information S1), high sampling rates (10 MHz) and time-dependent, anisotropic, layered velocity models generated from ultrasonic pulses emitted every 30 s. We searched for AE events within 100 μs time windows (resulting in peak rates of 10 ev/ms), and kept events with high signal-to-noise ratio, at least 8 station picks and travel time residuals of less than 0.5 μs, thereby minimizing the likelihood of erroneous detection and locations. AE location uncertainty was between 0.5 and 3 mm (Figure S6 in Supporting Information S1). We computed

local magnitudes based on peak AE amplitudes averaged across the entire array, corrected for source receiver distances (Zang et al., 1998) and assigned a minimum event size corresponding to the smallest grain size at the sub millimeter-scale (Blanke et al., 2020). The local magnitude scale provides good estimates of relative event sizes for the vast majority of the recorded AE events but likely underestimates the largest event magnitudes.

We evaluate potential effects of short-term incompleteness due to saturation of the seismic recording system. A comparison between AE rates and magnitudes for different slip events with intact rock fracture highlights that incomplete records are only a significant issue during rock fracture whereas slip on existing faults shows little evidence of incomplete records (Figure S5 in Supporting Information S1). This inference is also supported by the raw waveform records which show maximum duration of event-seismograms of about 0.1–0.2 s. This time window was excluded from the aftershock analyses.

2.3. Waiting Time Distributions and *R*-Ratios

We compare laboratory waiting time distributions with seismicity catalogs generated using a forward Epidemic-Type-Aftershock-Sequence (ETAS) approach that includes all key statistical relationships that govern earthquake triggering (Felzer et al., 2002). Both laboratory and ETAS waiting time distributions are well described by a two parameter Γ-distribution of the form: $p(\tau) \propto \tau^{\alpha-1}e^{-\tau/\beta}$, where τ are the interevent times between successive AE pairs and α and β are constants describing power-law decay at short times and background rates at large time scales. These parameters were determined using a maximum likelihood approach and the background rates were determined from $\lambda_0 = 1/\beta$ (Hainzl et al., 2006), which was confirmed by synthetic ETAS tests (Figure S10 in Supporting Information S1). Waiting time distributions for ETAS catalogs, laboratory and natural seismicity all collapse onto the same trend after normalizing by average interevent times, suggesting similar triggering behavior in lab and nature (Figure 2b).

To further test for systematic triggering in the lab, we determined interevent time ratios, R using:

$$R_i = \Delta t_{i+1}/(\Delta t_{i+1} - \Delta t_i), \tag{1}$$

where Δt_i and Δt_{i+1} are time intervals between successive event pairs and $i = 2, \ldots, N-1$. The probability density function of R is uniformly distributed between 0 and 1 for Poissonian rates and shows a significant peak at $R = 0$ in the presence of seismic triggering. This peak is a result of shorter than average time intervals, for example, within an aftershock sequence.

2.4. Empirical Stiffness and Slip Stability Estimates

Frictional sliding and the transition from stable sliding to stick-slip is affected by system stiffness. Stiffness, S, in our experiments refers to the combined axial loading stiffness of machine, fault and sample bulk, and was determined during axial loading and unloading at confining pressures between 120 and 150 MPa. We used the recorded axial stress for each experiment and determined S from the linear portion of stress over load point displacement prior to failure. Respective correlation coefficients are generally close to 0.99. We compared values between individual stick-slip cycles as well as stiffness during loading and unloading and used average values after outlier removal. Stiffness estimates were generally comparable between loading and unloading cycles at high confining pressures but may differ at lower confining pressure. The system stiffness for each experiment was generally lower than the estimated machine stiffness of ~350 MPa/mm.

Based on stiffness and normal stress, we determined a frictional stability parameter, γ, analogous to Leeman et al. (2016):

$$\gamma = S/S_c \quad \text{and} \quad S_c = \sigma_n(b-a)/D_c, \tag{2}$$

where $b - a$ are frictional rate-state parameters and D_c is the roughness-dependent characteristic weakening distance. For stick-slip to occur, the strength-reduction rate has to exceed elastic unloading (i.e., $S_c > S$). Values of γ below unity suggest increasingly unstable frictional behavior that favors sudden, large stress drops whereas values above one promote stable sliding.

We constrained frictional parameters by modeling dynamic slip on two representative experiments in 2-D plane strain using different self-affine surface roughness (see Tal et al., 2020, for details). Principal stresses in the

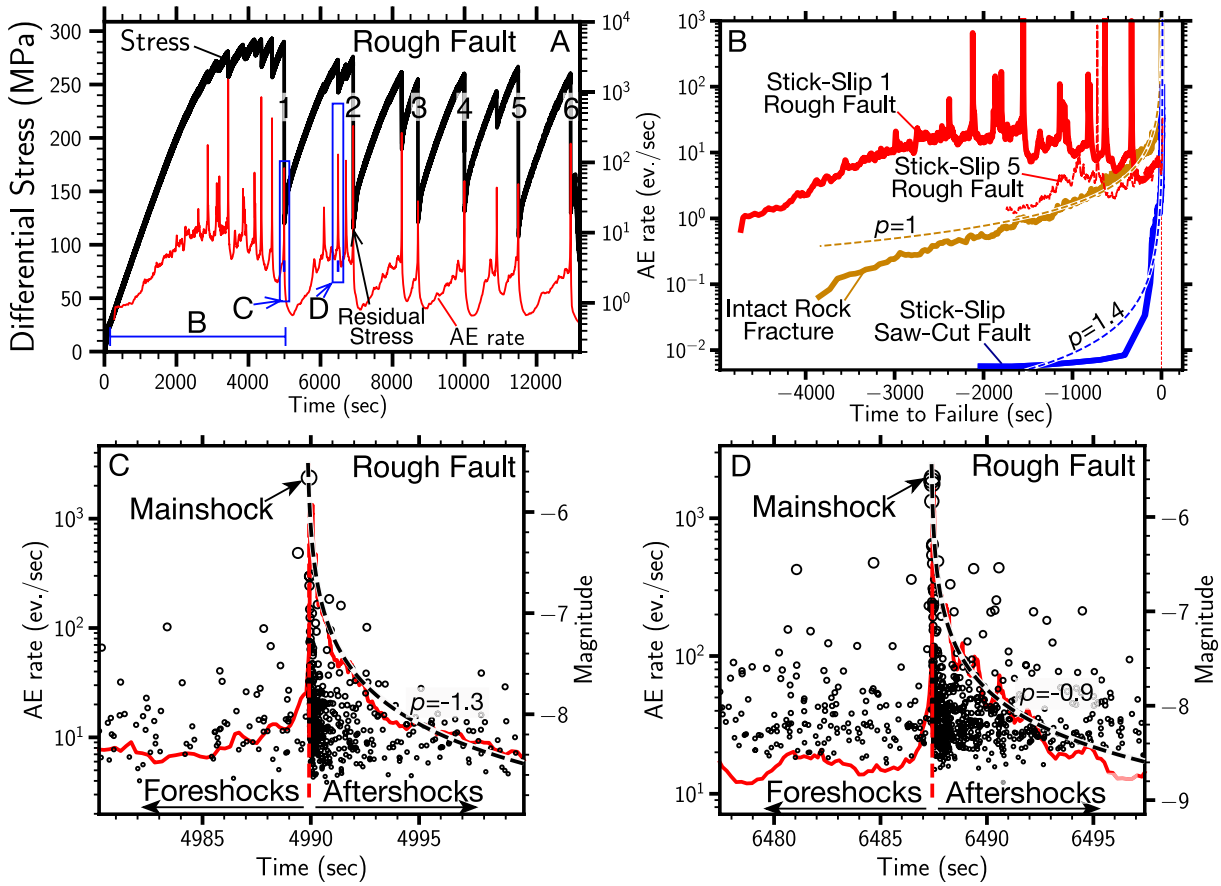

Figure 1. Acoustic emission (AE) rates exhibit pronounced spikes followed by gradual Omori-like decay during stick-slip on rough lab-faults whereas slip on smooth faults show little to no aftershocks. (a) Differential stress (black) and AE rates (red) during six large stress drop events on a rough fault, preceded by AE rate spikes that commonly coincide with small stress drop events. The blue bar and rectangles highlight time windows in (b), (c), and (d). (b) AE rates before large slip events on a smooth (blue) and rough fault (red) as well as before intact rock fracture (dark yellow). Both intact rock fracture and slip on smooth faults are preceded by nearly monotonous, power-law-like rate increase whereas slip on rough faults shows intermittent rate spikes and no clear increase before failure. (c), (d) Examples of Omori-fits (black dashed curves) to aftershock decay (red line) associated with a small (c) and large (d) stress drop event. AE magnitudes are shown as black circles. Note that here p-values indicate aftershock decay exponents where as p-value in B indicate exponents of inverse Omori relations leading up to failure.

numerical models matched those in the experiments. Similarly, we prescribed loading velocity at the lower boundary to match the experiments and then allow for spontaneous nucleation and evolution of slip events. We considered two interface geometries both with the same Hurst exponent ($H = 0.5$) but with different pre-factors, C, for rough ($C = 2 \times 10^{-6}$) and smooth faults ($C = 5 \times 10^{-8}$) which were determined by using white-light-interferometry. Surface friction in the numerical model was governed by a rate and state friction law with an aging evolution law combined with enhanced dynamic weakening in the form of flash heating (Tal et al., 2020). The observed variation in slip behavior between smooth and rough surfaces in the experiments was captured by varying D_c between 1 and 2 μm in the numerical models (Figure S11 in Supporting Information S1). These values are in good agreement with previous measurements of frictional parameters on Westerly granite surfaces (Mitchell et al., 2016).

3. Results

Triaxial loading of rough, heterogeneous lab-faults leads to a range of slip behavior and associated stress drops. We differentiate small and large slip events with measurable, macroscopic stress release (large slip events are labeled from 1 to 6 in Figure 1a). Small slip events only occur on rough faults close to peak stress and are characterized by shorter waiting times between events. Large slip events, on the other hand, occur on both rough and smooth faults, leading to significant stress release and longer waiting times between subsequent large events. Large slip events on rough faults occur at similar or at times even slightly lower stresses than the preceding small

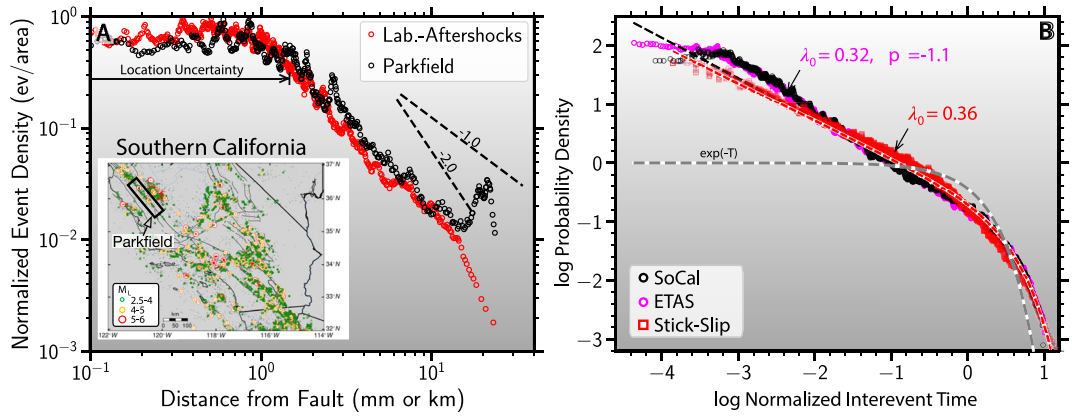

Figure 2. Spatial and temporal clustering of laboratory acoustic emission events on rough faults is similar to natural seismicity clustering and indicate efficient short-term triggering. (a) Spatial decay of microseismicity as a function of distance from a lab fault (red) and the San Andreas fault at Parkfield (black). Inset shows location of the Parkfield segment and earthquake clusters in Southern California used in (b), colored by mainshock magnitude (see legend). A larger version of the map is shown in Figure S9 in Supporting Information S1. (b) Interevent times and Γ-distribution fits for Southern California (black) and laboratory (red) seismicity and seismicity generated by forward Epidemic-Type-Aftershock-Sequence (ETAS) (magenta) modeling (background fraction, $\lambda_0 = 0.32$, Omori exponent, $p = -1.1$). Note that ETAS parameters were originally chosen to match Southern California seismicity but also match the laboratory observations.

stress drop events (see event 3, Figure 1a). The difference in slip behavior on smooth and rough faults are likely a result of higher levels of stress heterogeneity before and after slip on rough faults (T. H. W. Goebel et al., 2017). Slip events are generally accompanied by small, high-frequency and impulsive AE events which we cataloged and characterized based on full waveform records (Figure S4 in Supporting Information S1).

We observe that rough faults show much more complex AE rate changes than the fracture of intact-rock or slip on smooth faults (Figure S7 in Supporting Information S1). Intact rock fracture and smooth faults can be characterized by monotonous AE event acceleration to failure. Both AE rates and seismic moment release for these experiments show a power-law increase with time-to-failure (Figure 1b; Figure S2 in Supporting Information S1). For rough faults, AE rate and moment release do not show this simple power law behavior but rather an early acceleration followed by extended periods of consistently-high rates and moment release (Figure S2 in Supporting Information S1).

The preparatory phase before large stress drop events on rough faults—which includes seismic and aseismic deformation (Dresen et al., 2020)—is characterized by intermittent macroscopic slip and bursts of high-frequency AE events. A closer inspection of such rate spikes demonstrates that they are comprised of mainshock-aftershock sequences, that is, seismic sequences with one or several large-magnitude events followed by smaller magnitude events with Omori-like rate decrease with time (Figures 1c and 1d). Notably, both small and large slip events are accompanied by relaxation processes that lead to Omori-like rate decay over 1–10 s (Figure S3 in Supporting Information S1). Based on the observed Omori-like decay, we refer to AE events within ∼10 s after slip events as aftershocks. Aftershocks are commonly distributed across the entire lab-fault immediately after AE mainshocks, even when macroscopic stress release is small (Figure S8 in Supporting Information S1).

We verify the reliability of respective AE event detection by examining full waveform records and ruling out biases due to short-term incompleteness (Figure S5 in Supporting Information S1). Macroscopic slip events start abruptly and continue as a more gradual strain relaxation process with a duration that depends on the overall stress release during slip (Figure S3 in Supporting Information S1). The superposition of intermittent, abrupt slip and gradual relaxation processes are remarkably different from previously observed simple AE acceleration toward failure (e.g., Meredith et al., 1990) and highlight a distinct pattern of seismic energy partitioning within seismic sequences, including pronounced aftershock contributions.

To explore potential parallels between lab and nature, we compare spatial seismicity distributions across strike-slip faults in southern California to spatial clustering on rough lab-faults. We isolate aftershock activity within 5 s of all small and large slip events and calculate event density decay as a function of fault normal distance. This spatial decay can be described by a power-law at distances between 1 and 10 mm analogously to seismicity

distributions across the Parkfield segment of the San Andreas fault (Figure 2a) (T. H. W. Goebel, Becker, et al., 2014; T. H. W. Goebel, Candela, et al., 2014). Previous studies found that seismicity density profiles vary across different strike-slip faults in California but generally show similar high event-density plateaus toward the fault core followed by a power-law decay to maximum distances of 1–10 km (Powers & Jordan, 2010), which matches the here described lab-observations.

Similarly to spatial seismicity clustering, temporal clustering of all AE events on rough faults in the lab can be described by the same statistical distribution function (i.e., a Γ-distribution) as natural earthquakes. We find that short interevent times of lab AEs are dominated by power-law decay that matches Omori-type aftershock clustering in synthetic ETAS-catalogs (Figure 2b), indicating similar underlying event interactions. Longer inter-event times exhibit a transition to Poissonian background rates with comparable fractions of background events, λ_0, based on two-parameter Γ-distribution fits. The combination of short-term power-law decay and long-term Poissonian rates mirrors natural seismicity statistics and is markedly different from smooth faults and intact rock fracture which lack either short-term clustering or Poissonian background (Figure S10b in Supporting Information S1).

Differences in temporal clustering are even more pronounced when comparing *R*-statistics of interevent-time ratios between the different experiments (Figure S10c in Supporting Information S1). Seismic events on rough faults and in nature show evidence of triggering in form of distribution peaks at small *R*-values. Intact-rock fracture and slip on smooth faults, on the other hand, lack such short-term interactions in spite of rate-acceleration toward failure. Taken together, the observed space-time clustering on rough faults mirrors seismic event distributions in nature.

We further quantify temporal event clustering in the laboratory by calculating the aftershock productivity after each slip event. We determine aftershock productivity, *K*, by integrating the modified Omori-Utsu relationship ($dN/dt = K/(c + t)^p$) and counting the relative increase in number of AE events, *N* within 2 s after, compared to 2 s before slip onset. We isolate variations in *K* by leaving *c* and *p* constant and find that respective aftershock productivity variations are correlated with residual stress, through:

$$K \propto \tau_{\text{res}}^{\beta}, \tag{3}$$

where β is a scaling exponent and τ_{res} is the remaining shear stress on the fault after rapid slip events (Figure 3). This correlation is consistently observed across a range of completeness magnitudes and aftershock time windows (Figures S14 and S15 in Supporting Information S1). For values of $\beta = 2$ as indicated in (Figure 3b), we find that *K* is linearly related to, *e*, the residual strain energy per volume (in [Nm/m^3]) after slip with:

$$e = \tau_{\text{res}}^2/G, \tag{4}$$

where *G* is the shear modulus. This relationship provides a simple physical underpinning for the observed relationship, suggesting that mainshocks with comparably small displacements and high remaining strain energy promote productive aftershock sequences.

In addition to high residual stress, high aftershock productivity is also promoted by larger fault roughness and associated, more pervasive fault damage (Figure 3b). Aftershocks are almost completely absent on smooth faults which exhibit little damage in postmortem thin-sections. We conclude that residual stress and fault roughness are the key parameters that control aftershock productivity in our tests.

To better understand the primary controls on residual stress after slip, we employ a simple model for the mechanics of stick-slip that is based on rate-dependent friction and system stiffness, *S*. The fault mechanical behavior in our experiments is controlled by a slip stability parameter, $\gamma = S/S_c$ (see Method). Small values of $\gamma < 0.9$ promote slip instability due to more rapid strength reduction compared to elastic unloading (Figure 3a). Larger values of $\gamma > 1.25$ promote stable sliding with occasional small slip events on rough faults. In between these two regimes, we observe a transitional regime which is marked by both small and large slip events. The associated AE events exhibit strong space-time clustering, analogous to natural seismicity, and aftershock triggering is amplified.

The combined effects of fault roughness (or D_c), normal stress and stiffness variations explain the observed spectrum of average slip behavior (Figure 3a), albeit the individual variables have limited predictive power (Figure S12 in Supporting Information S1). For instance, aftershock productivity increases with larger normal stress but only when examining smooth and rough faults separately and there are also significant trade-offs with

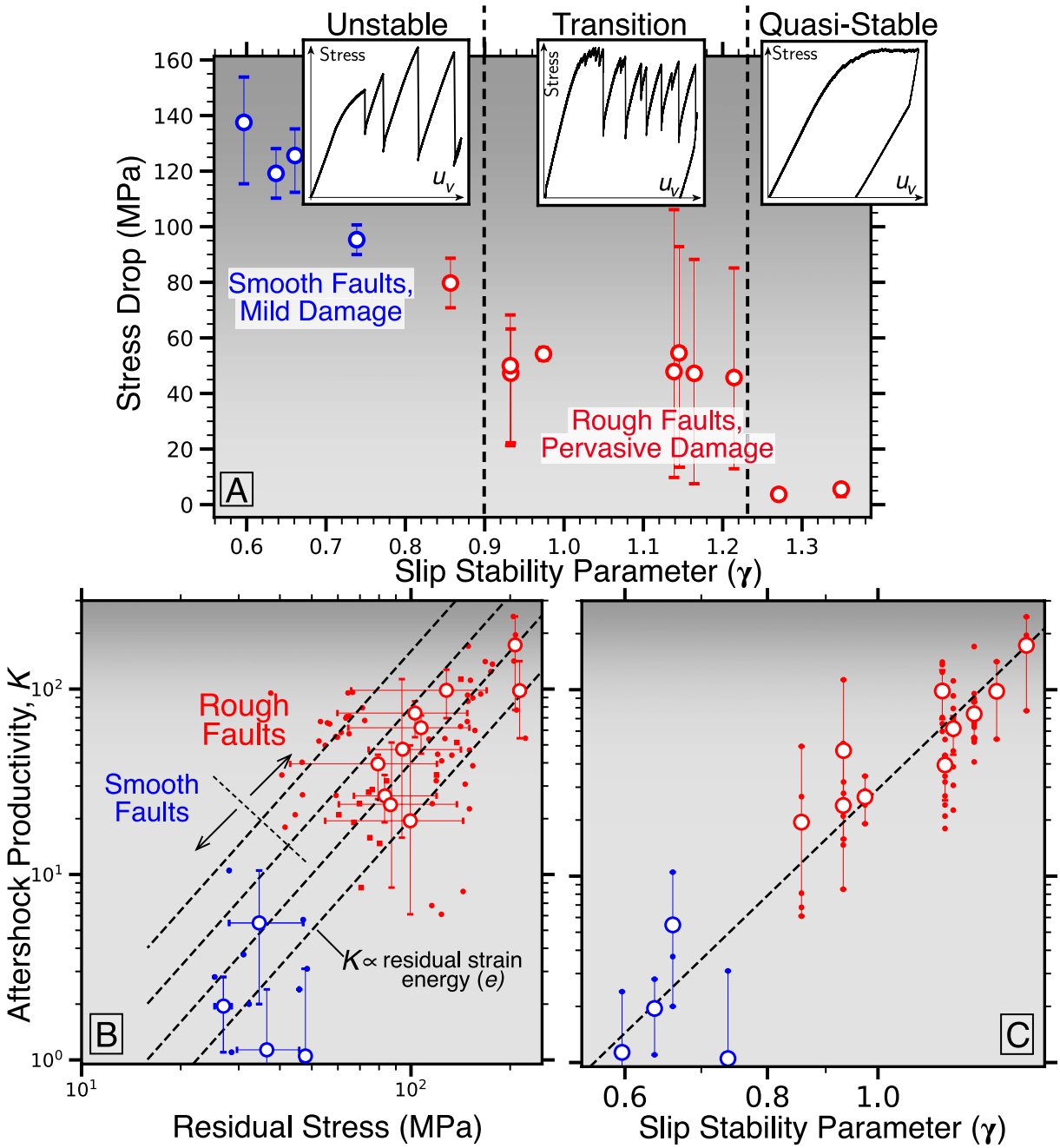

Figure 3. Aftershock productivity is strongly affected by residual stress after slip. (a) Stress drop is controlled by a slip stability parameter (see text), with smooth faults (blue) generally exhibiting higher stress drops than rough faults (red). Insets show exemplary axial stress over displacement curves separated into unstable ($\gamma < 0.9$), transitional ($\gamma = 0.9$–1.25) and quasi-stable ($\gamma > 1.25$) regimes. (b) Aftershock productivity as a function of residual stress for rough (red) and smooth (blue) faults. Large markers represent averages for entire experimental runs, small markers show results for individual small and large slip events. Dashed line indicates a potential quadratic dependence of productivity on stress (see text). (c) Aftershock productivity as a function of slip stability, γ. Dashed line shows least-squares fit of K and γ in log-space. Error bars in all panels show 10th and 90th percentiles or the full data range if fewer than five slip events were recorded.

stiffness (Figure S13 in Supporting Information S1). Within the group of rough-fault experiments, system stiffness reduction promotes slip instability and fewer aftershocks. This reduction in stiffness was accomplished by increasing the length of the 30° notches that guided the subsequent fracture process (Figure S1 in Supporting Information S1). We find that lower roughness and stiffness both favor unstable sliding (i.e., stick-slip) at confining pressures between 120 and 150 MPa, whereas slip on rough faults without notches was always stable at the same confining pressures.

4. Discussion

Our results highlight that not only mainshock stress transfer but also geometric heterogeneity are important during aftershock triggering. The effect of surface roughness on aftershock generation has previously been predicted by theoretical models of rough faults governed by rate-and-state friction (J. H. Dieterich & Smith, 2009). Such numerical models predict stress concentrations due to inhomogeneous slip on rough faults, which are released in form of brittle failure, that is, aftershocks, within the fault damage zone (Powers & Jordan, 2010). Interestingly, frictional constitutive relations for fault populations without roughness-effects predict that larger stress steps promote higher aftershock productivity (J. Dieterich, 1994). We observe the opposite, that is, higher stress drop and lower residual stress leading to fewer aftershocks compared to low stress drop events. Aftershock triggering in nature is likely to be still more complex due to far-field stress transfer and triggering outside of the ruptured area.

Observations of systematic aftershock deficiency in areas of high co-seismic slip have been made for some natural faults (Dascher-Cousineau et al., 2020; Ross et al., 2019; Wetzler et al., 2018). The underlying conditions for low aftershock activity may be a combination of low fault roughness, normal stress and system stiffness, ultimately leading to high stress release during the mainshock (Figure 4).

We observe that preparatory processes before slip on smooth faults are associated with foreshocks and a pronounced asymmetry in seismic sequence partitioning that are depleted in aftershocks. Similarly, laboratory rock fracture is dominated by precursory signals and foreshocks but little to no aftershocks (Meredith et al., 1990). This partitioning is the opposite in nature where foreshocks are rare and aftershocks dominate. Our experiments on rough faults, on the other hand, generate pronounced aftershock activity and seismic sequence partitioning analogous to natural seismicity. This analogy between natural and lab seismicity may be governed by fault roughness which exhibits similar scaling relations from micrometers to meters and Hurst exponents between 0.5 and 0.65 (Candela et al., 2012; T. H. W. Goebel et al., 2017) (Figure 4c).

Rougher faults with large geometric complexity exhibit a range of slip behavior including small and large stress drop events and aftershock productivity that is one to two orders of magnitude larger than on smooth faults. Average productivity for each experiment is well-explained by the residual strain energy on the fault after slip. The correlation between K and strain energy is much weaker when analyzing similarly-rough faults suggesting that differences in roughness and heterogeneity are more dominant than ambient stress effects (Figure S16 in Supporting Information S1). Fault roughness may, thus, be of primary importance for aftershock productivity and general seismic behavior including earthquake magnitude distributions (T. H. W. Goebel et al., 2017). In addition to differences in roughness, seismic behavior may also be affected by fault damage properties and strain localization based on observed off-fault activity which extends out to ∼6 mm on smooth and ∼1 cm on rough faults (T. H. W. Goebel, Becker, et al., 2014; T. H. W. Goebel, Candela, et al., 2014). The faults with broader damage zones around rough surfaces are associated with much higher aftershock productivity. Fully resolving the trade-offs between roughness and damage will require addition testing.

We note that there are several limitations to the current set of experiments. Static and dynamic stress transfer, for example, can only be studied in the near-field (within ∼0.5 rupture dimensions) because the lab tests are limited by finite sample size and fault length. As a consequence, the relative importance of stress transfer ahead of the rupture and at large distances is difficult to assess in the lab. Moreover, the triaxial set-up permits only small cumulative fault offsets so that surface evolution is limited. We see some indication of surface smoothing with successive large slip events expressed by decreasing AE off-fault activity and residual stresses and fewer small stress drop events. Slip on natural faults likely leads to surface smoothing as well as re-roughening and damage generation for example, caused by large dynamic strain, bi-material interfaces, fault step-overs and branching (Brodsky et al., 2011; Faulkner et al., 2010).

5. Conclusion

Stick-slip has been accepted as a mechanism for earthquakes since the seminal work by Brace and Byerlee in the 1960's (Brace & Byerlee, 1966). Our results suggest that the originally proposed large stress drop events on highly unstable faults are unlikely to produce many aftershocks close to the ruptured fault patch. Instead, laboratory seismicity clustering and aftershock behavior similar to nature are promoted by large surface roughness and

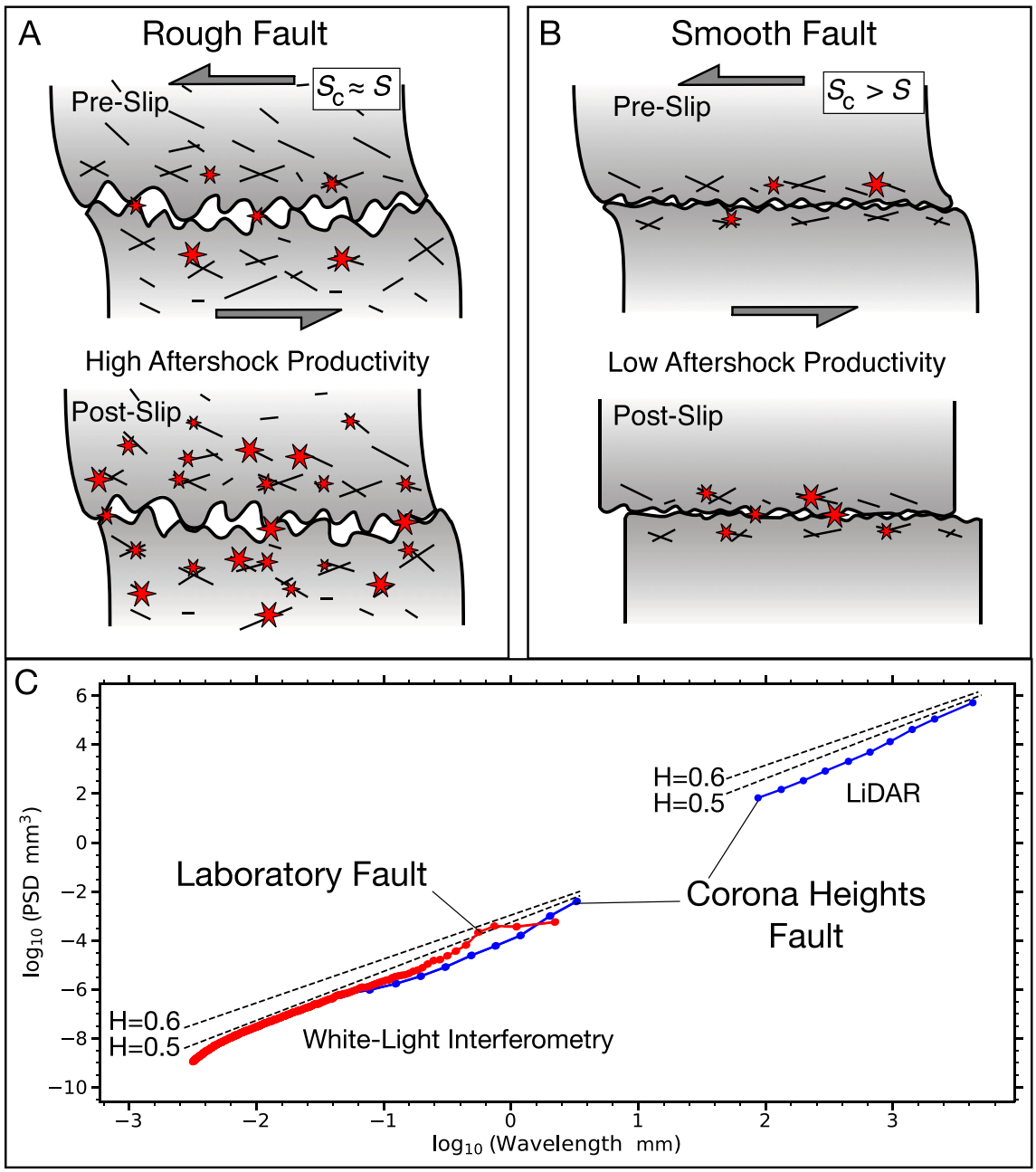

Figure 4. Schematic representation of slip and aftershocks on rough (a) and smooth (b) faults with moderate and pervasive damage. (a) Aftershock activity is amplified by larger fault roughness and damage when the strength-reduction rate, S_c is similar to the elastic unloading stiffness, S. (b) Smooth faults with $S_c > S$ generate very few aftershocks and most of the stored strain is released during the mainshock. (c) Roughness measurements suggest a similar scaling of Power-Spectral-Density (PSD) and wavelength in lab (red) and nature (blue) with Hurst exponents between 0.5 and 0.65. The natural fault measurements are averaged PSDs from LiDAR, and white-light interferometric scans of the Corona Heights fault in California, resampled using log-bins (modified from Candela et al., 2012).

heterogeneity at conditions not far from slip instability. The experiments provide fundamental insight into seismic sequence partitioning which, in the lab, is driven by accelerating and decelerating stress relaxation processes before and after the main slip event. The relaxation process starts close to peak stress and involves both preparatory slip and foreshocks as well as aftershocks. The underlying mechanics of slip are controlled by fault roughness, system stiffness and normal stress.

Aftershock generation in the natural system is strongly affected by mainshock characteristics. Our lab tests suggest that, in addition to mainshock stresses, fault roughness and damage zone stiffness need to be considered.

We find that aftershock productivity, K, is linearly related to the remaining elastic energy density after slip with $K = C \times \tau_{res}^2/G$, where C is a constant and G is the shear modulus. This relationship suggests that heterogeneous fault patches with high remaining strain energy promote productive aftershock sequences. Documenting differences in fault zone properties such as roughness and damage may thus improve the overall understanding of aftershock triggering.

Conflict of Interest

The authors declare no conflicts of interest relevant to this study.

Data Availability Statement

All data is available at: https://data.mendeley.com/datasets/t2cht66xpr/1 (T. Goebel, 2022).

Acknowledgments
The authors would like to thank Grzegorz Kwiatek for comments and discussions, and Stefan Gehrmann and Matthias Kreplin for rock sample preparation at GFZ-Potsdam, Germany. The manuscript benefited from thoughtful reviews by Deborah Smith, John Leeman, Greg McLaskey and Marco Scuderi. This research was made possible by a Humboldt fellowship to Goebel, an NSF Career Award (Award Number: 2142489) and an USGS NEHRP grant (G21AP10050).

References

Ben-Zion, Y., & Lyakhovsky, V. (2006). Analysis of aftershocks in a lithospheric model with seismogenic zone governed by damage rheology. *Geophysical Journal International*, *165*(1), 197–210. https://doi.org/10.1111/j.1365-246X.2006.02878.x

Blanke, A., Kwiatek, G., Goebel, T. H. W., Bohnhoff, M., & Dresen, G. (2020). Stress drop–magnitude dependence of acoustic emissions during laboratory stick-slip. *Geophysical Journal International*, *224*(2), 1371–1380. https://doi.org/10.1093/gji/ggaa524

Brace, W., & Byerlee, J. (1966). Stick-slip as a mechanism for earthquakes. *Science*, *153*(3739), 990–992. https://doi.org/10.1126/science.153.3739.990

Brodsky, E. E., Gilchrist, J. J., Sagy, A., & Collettini, C. (2011). Faults smooth gradually as a function of slip. *Earth and Planetary Science Letters*, *302*(1–2), 185–193. https://doi.org/10.1016/j.epsl.2010.12.010

Candela, T., Renard, F., Klinger, Y., Mair, K., Schmittbuhl, J., & Brodsky, E. E. (2012). Roughness of fault surfaces over nine decades of length scales. *Journal of Geophysical Research*, *117*(B8). https://doi.org/10.1029/2011JB009041

Dascher-Cousineau, K., Brodsky, E. E., Lay, T., & Goebel, T. H. W. (2020). What controls variations in aftershock productivity? *Journal of Geophysical Research: Solid Earth*, *125*(2), 1–18. https://doi.org/10.1029/2019JB018111

Davidsen, J., Kwiatek, G., Charalampidou, E.-M., Goebel, T., Stanchits, S., Rück, M., & Dresen, G. (2017). Triggering processes in rock fracture. *Physical Review Letters*, *119*(6), 068501. https://doi.org/10.1103/PhysRevLett.119.068501

Dieterich, J. (1994). A constitutive law for rate of earthquake production and its application to earthquake clustering. *Journal of Geophysical Research*, *99*(B2), 2601–2618. https://doi.org/10.1029/93JB02581

Dieterich, J. H., & Smith, D. E. (2009). Nonplanar faults: Mechanics of slip and off-fault damage. *Pure and Applied Geophysics*, *166*(10–11), 1799–1815. https://doi.org/10.1007/s00024-009-0517-y

Dresen, G., Kwiatek, G., Goebel, T., & Ben-Zion, Y. (2020). Seismic and aseismic preparatory processes before large stick–slip failure. *Pure and Applied Geophysics*, *177*(12), 5741–5760. https://doi.org/10.1007/s00024-020-02605-x

Ellsworth, W. L., & Bulut, F. (2018). Nucleation of the 1999 Izmit earthquake by a triggered cascade of foreshocks. *Nature Geoscience*, *11*(7), 531–535. https://doi.org/10.1038/s41561-018-0145-1

Elst, N. J. V. D., & Brodsky, E. E. (2010). Connecting near-field and far-field earthquake triggering to dynamic strain. *Journal of Geophysical Research*, *115*, 1–21. https://doi.org/10.1029/2009JB006681

Faulkner, D. R., Jackson, C. A. L., Lunn, R. J., Schlische, R. W., Shipton, Z. K., Wibberley, C. A. J., & Withjack, M. O. (2010). A review of recent developments concerning the structure, mechanics and fluid flow properties of fault zones. *Journal of Structural Geology*, *32*(11), 1557–1575. https://doi.org/10.1016/j.jsg.2010.06.009

Felzer, K. R., & Brodsky, E. E. (2006). Decay of aftershock density with distance indicates triggering by dynamic stress. *Nature*, *441*(7094), 735–738. https://doi.org/10.1038/nature04799

Felzer, K. R., Becker, T. W., Abercrombie, R. E., Ekström, G., & Rice, J. R. (2002). Triggering of the 1999 M_W 7.1 Hector Mine earthquake by aftershocks of the 1992 M_W 7.3 Landers earthquake. *Journal of Geophysical Research*, *107*(B9), 2190. https://doi.org/10.1029/2001JB000911

Goebel, T. (2022). Fault roughness and laboratory aftershocks [dataset]. Mendeley Data. https://doi.org/10.17632/t2cht66xpr.1

Goebel, T. H. W., Becker, T. W., Sammis, C. G., Dresen, G., & Schorlemmer, D. (2014). Off-fault damage and acoustic emission distributions during the evolution of structurally complex faults over series of stick-slip events. *Geophysical Journal International*, *197*(3), 1705–1718. https://doi.org/10.1093/gji/ggu074

Goebel, T. H. W., Candela, T., Sammis, C. G., Becker, T. W., Dresen, G., & Schorlemmer, D. (2014). Seismic event distributions and off-fault damage during frictional sliding of saw-cut surfaces with pre-defined roughness. *Geophysical Journal International*, *196*(1), 612–625. https://doi.org/10.1093/gji/ggt401

Goebel, T. H. W., Kwiatek, G., Becker, T. W., Brodsky, E. E., & Dresen, G. (2017). What allows seismic events to grow big?: Insights from b-value and fault roughness analysis in laboratory stick-slip experiments. *Geology*, *45*(9), 815–818. https://doi.org/10.1130/G39147.1

Hainzl, S., Scherbaum, F., & Beauval, C. (2006). Estimating background activity based on interevent-time distribution. *Bulletin of the Seismological Society of America*, *96*(1), 313–320. https://doi.org/10.1785/0120050053

Helmstetter, A., & Sornette, D. (2003). Foreshocks explained by cascades of triggered seismicity. *Journal of Geophysical Research*, *108*(B10), 20. https://doi.org/10.1029/2003JB002409

Kanamori, H., & Brodsky, E. E. (2004). The physics of earthquakes. *Reports on Progress in Physics*, *67*(8), 1429–1496. https://doi.org/10.1088/0034-4885/67/8/R03

King, G., King, C., Stein, R. S., & Lin, J. (1994). Static stress changes and the triggering of earthquakes. *Bulletin of the Seismological Society of America*, *84*, 935–953. https://doi.org/10.1016/0148-9062(95)94484-2

Kwiatek, G., Plenkers, K., & Dresen, G. (2011). Source parameters of picoseismicity recorded at Mponeng deep gold mine, South Africa: Implications for scaling relations. *Bulletin of the Seismological Society of America*, *101*(6), 2592–2608. https://doi.org/10.1785/0120110094

Leeman, J. R., Saffer, D. M., Scuderi, M. M., & Marone, C. (2016). Laboratory observations of slow earthquakes and the spectrum of tectonic fault slip modes. *Nature Communications*, *7*(1), 11104. https://doi.org/10.1038/ncomms11104

McLaskey, G. C., Kilgore, B. D., Lockner, D. A., & Beeler, N. M. (2014). Laboratory generated M -6 earthquakes. *Pure and Applied Geophysics*, *171*(10), 2601–2615. https://doi.org/10.1007/s00024-013-0772-9

Meredith, P. G., Main, I. G., & Jones, C. (1990). Temporal variations in seismicity during quasi-static and dynamic rock failure. *Tectonophysics*, *175*(1–3), 249–268. https://doi.org/10.1016/0040-1951(90)90141-t

Mitchell, E. K., Fialko, Y., & Brown, K. M. (2016). Velocity-weakening behavior of westerly granite at temperature up to 600°C. *Journal of Geophysical Research: Solid Earth*, *121*(9), 6932–6946. https://doi.org/10.1002/2016JB013081

Perfettini, H., & Avouac, J.-P. (2004). Postseismic relaxation driven by brittle creep: A possible mechanism to reconcile geodetic measurements and the decay rate of aftershocks, application to the Chi-Chi earthquake, Taiwan. *Journal of Geophysical Research*, *109*(B2), 1–15. https://doi.org/10.1029/2003jb002488

Powers, P. M., & Jordan, T. H. (2010). Distribution of seismicity across strike-slip faults in California. *Journal of Geophysical Research*, *115*(B5), B05305. https://doi.org/10.1029/2008JB006234

Ross, Z. E., Idini, B., Jia, Z., Stephenson, O. L., Zhong, M., Wang, X., et al. (2019). Hierarchical interlocked orthogonal faulting in the 2019 Ridgecrest earthquake sequence. *Science*, *3665*(6463), 346–351. https://doi.org/10.1126/science.aaz0109

Scholz, C. H. (1968). Microfractures, aftershocks, and seismicity. *Bulletin of the Seismological Society of America*, *58*, 1117–1130.

Stanchits, S., Vinciguerra, S., & Dresen, G. (2006). Ultrasonic velocities, acoustic emission characteristics and crack damage of basalt and granite. *Pure and Applied Geophysics*, *163*(5–6), 975–994. https://doi.org/10.1007/s00024-006-0059-5

Tal, Y., Goebel, T., & Avouac, J.-P. J.-P. (2020). Experimental and modeling study of the effect of fault roughness on dynamic frictional sliding. *Earth and Planetary Science Letters*, *536*, 116133. https://doi.org/10.1016/j.epsl.2020.116133

Utsu, T. (1999). Representation and analysis of the earthquake size distribution: A historical review and some approaches. *Pure and Applied Geophysics*, *155*(2–4), 509–535. https://doi.org/10.1007/s000240050276

Wetzler, N., Lay, T., Brodsky, E. E., & Kanamori, H. (2018). Systematic deficiency of aftershocks in areas of high coseismic slip for large subduction zone earthquakes. *Science Advances*, *4*(2), eaao3225. https://doi.org/10.1126/sciadv.aao3225

Zaliapin, I., & Ben-Zion, Y. (2013). Earthquake clusters in southern California I: Identification and stability. *Journal of Geophysical Research: Solid Earth*, *118*(6), 2847–2864. https://doi.org/10.1002/jgrb.50179

Zang, A., Wagner, F. C., Stanchits, S., Dresen, G., Andresen, R., & Haidekker, M. A. (1998). Source analysis of acoustic emissions in Aue granite cores under symmetric and asymmetric compressive loads. *Geophysical Journal International*, *135*(3), 1113–1130. https://doi.org/10.1046/j.1365-246x.1998.00706.x